Geomorphology 123 (2010) 257–268

Contents lists available at ScienceDirect

Geomorphology

journal homepage: www.elsevier.com/locate/geomorph

El Niño forcing on ^{10}Be-based surface denudation rates in the northwestern Peruvian Andes?

Luca M. Abbühl [a,1], Kevin P. Norton [a,*], Fritz Schlunegger [a], Oliver Kracht [a], Ala Aldahan [b,c], Göran Possnert [d]

[a] Institute of Geological Sciences, University of Bern, Baltzerstr. 1+3, CH-3012 Bern, Switzerland
[b] Department of Earth Sciences, Uppsala University, SE-752 36 Uppsala, Sweden
[c] Department of Geology, United Arab Emirates University, Al Ain, United Arab Emirates
[d] Tandem Laboratory, Uppsala University, SE-751 20 Uppsala, Sweden

ARTICLE INFO

Article history:
Received 22 March 2010
Received in revised form 19 July 2010
Accepted 22 July 2010
Available online 3 August 2010

Keywords:
Northwestern Peruvian Andes
El Niño
^{10}Be denudation rates
Landscape transience

ABSTRACT

High magnitude precipitation events provide large contributions to landscape formation and surface denudation in arid environments. Here, we quantify the precipitation-dependent geomorphic processes within the Rio Piura drainage basin located on the Western Escarpment of the northern Peruvian Andes at 5°S latitude. In this region, monsoonal easterly winds bring precipitation to the >3000 m asl high headwaters, from where the annual amount of precipitation decreases downstream toward the Pacific coast. Denudation rates are highest in the knickzones near the headwaters, ~200–300 mm ky^{-1}, and sediment discharge is limited by the transport capacity of the channel network. Every few years, this situation is perturbed by westerly, wind-driven heavy precipitation during El Niño events and results in supply-limited sediment discharge as indicated by bedrock channels.

The detailed analysis of the stream-long profiles of two river basins within the Rio Piura catchment reveals a distinct knickzone in the transition zone between the easterly and westerly climatic influences, suggesting an En Niño forcing on the longitudinal channel profiles over at least Holocene timescales. Measured trunk stream catchment-wide denudation rates are up to ca. 300 mm ky^{-1} and decrease successively downstream along the river profiles. Denudation rates of tributary rivers are ca. 200 mm ky^{-1} near the plateau and show a stronger downstream decreasing trend than trunk stream rates. This suggests that the landscape is in a transient stage of local relief growth, which is driven by fluvial incision. This corroborates the results of paleoclimate studies that point towards higher El Nino frequencies during the past ca. 3000 years, leading to higher runoff and more erosion in the trunk channel compared to the hillslopes and thus growth of local relief. Downstream increases in channel gradient spatially coincide with the reaches of highest precipitation rates during El Niño events, we therefore interpret that Holocene landscape evolution has largely been controlled by climate. The ky-timescale of the ^{10}Be data together with the transience of the landscape implies that El Niño events in northwestern Peru have occurred since at least the Holocene, and that adjustment to channel incision is still taking place.

1. Introduction

The relationship between hillslope and channel erosion and sediment transport has become an increasingly important research field during the past years with the development of higher resolution topographic data and chronometers. Among the first major research directions was the search for a link between climate and erosion. Based on apatite (U–Th)/He cooling ages from the Washington Cascades, Reiners et al. (2003) illustrated a close relationship between the pattern of surface erosion and modern precipitation rates, while Burbank et al. (2003) showed that erosion and precipitation have been decoupled in the Himalayas during geologic time scales. Dadson et al. (2003) also showed that erosion rates are strongly coupled with variations in precipitation and seismicity in the Taiwan orogen. Finer-scale studies have also recognized that climate plays an important role in scaling fluvial and hillslope erosion rates (e.g., Summerfield and Hulton, 1994; Reiners et al., 2003). In addition, Riebe et al. (2004) used cosmogenic radionuclides from different sites in the USA to illustrate that chemical weathering intensity varies systematically with climate. Similarly, for the Western Escarpment of the Andes of northern Chile, Kober et al. (2007, 2009) found a consistent relationship between precipitation and surface erosion rates. However, von Blanckenburg et al. (2004) concluded that, in the steep

* Corresponding author.
E-mail addresses: luca@geo.unibe.ch (L.M. Abbühl), kevin.norton@geo.unibe.ch (K.P. Norton).
[1] Tel.: +41 31 631 8775; fax: +41 31 631 4843.

0169-555X/$ – see front matter © 2010 Elsevier B.V. All rights reserved.
doi:10.1016/j.geomorph.2010.07.017

tropical highlands of Sri Lanka, erosion rates do not to depend on climate (see also von Blanckenburg, 2005). The emerging view is that, in the absence of landscape rejuvenation (e.g., a tectonic forcing, base-level fall, etc.), physical erosion rates are low (von Blanckenburg et al., 2004) and are nearly independent of precipitation rates, hillslope angles or local relief (e.g., Riebe et al., 2000). These tectonic perturbations on landscape are expressed by transient features of which knickzones in stream-long profiles are prominent examples (e.g., Whipple, 2004). Hillslopes adjacent to these knickzones often expose bedrock, which promotes sediment production by weathering (Cox, 1980; Heimsath et al., 1997).

The relative contributions of regolith production on hillslopes and removal by channelized processes shape the landscape (e.g. van der Beek and Braun, 1998; Perron et al., 2008). For instance, based on a detailed study carried out in the Finisterre Mountains of Papua New Guinea, Hovius et al. (1998) found that hillslope mass wasting at channel heads governs the rate and the mode of drainage basin modification. Other researchers have proposed that climate-driven fluvial erosion and sediment transport exerts a first-order control because fluvial processes are anticipated to set the lower boundary conditions for geomorphic processes on the adjacent slopes (e.g., Whipple et al., 1999; and review article by Whipple, 2004). Accordingly, increasing (or decreasing) rates of fluvial erosion result in equivalent modifications of local relief and, hence, in enhanced (or reduced) rates of erosion on the adjacent hillslopes (Tucker and Slingerland, 1997). It has also been recognized that large-magnitude flood events are important contributors to the total erosional mass flux from a basin (Wolman and Miller, 1960). For instance, Kirchner et al. (2001) stated that continuous incremental erosion only accounts for a small fraction of the total sediment yield in the Idaho Mountains and that, by contrast, rare and brief catastrophic erosion events dominate the long-term (10 ky and 10 my timescales) sediment yield. Similarly, Molnar (2001) assigned accelerated erosion to episodic large floods during which rivers exceed a threshold flow strength to transport bedload and to incise into bedrock.

High magnitude climatic perturbations in the form of westerly-driven El Nino events episodically affect the Western Escarpment in northern Peru. These contrast to the normal monsoonal precipitation pattern associated with easterly winds (Rasmusson and Carpenter, 1982; Rein, 2007; Bookhagen and Strecker, 2008; Fig. 1). Because of these climate contrasts, catchments in northern Peru, and particularly the Pirua drainage basin have been home to detailed geomorphic studies with the aim of detecting the landscape response to this dual climate (Schneider et al., 2008; Mettier et al., 2009). These studies converge on the general notion that landscape metrics and the limits on sediment discharge change with contrasts between the monsoonal and El Nino precipitation intensities. Given the results of these previous studies, we quantify the different erosional responses to this dual climate using concentrations of ^{10}Be in river born sand (Brown et al., 1995; Bierman and Steig, 1996; Granger et al., 1996).

We focus our analysis on two ca. 50 km^2 large transverse catchments (namely the Rio Yapatera and the Rio Las Gallegas) that are part of the Rio Piura drainage basin (Fig. 2). These transverse catchments were selected because they cover the full ranges of hillslope and channel gradients and climate in the area as detailed by Schneider et al. (2008) and Mettier et al. (2009). Because lithologic and tectonic conditions are approximately spatially uniform within the investigated area, the observable variation of denudation rates can be attributed solely to the influence of climate variation.

2. Settings

2.1. Climate

Along the Pacific coast in northern Peru, sinking air and the cold Peru (Humboldt) Current establish persistently cold and dry high pressure conditions (Woodman, 1998), hindering westerly precipitation from reaching the coast. Precipitation in the headwaters of the western Peruvian rivers is controlled by the positions of the Intertropical Convergence Zone (ITCZ) and the subtropical jet stream (Garreaud et al., 2003). During austral summer (December to February), the southernmost location of the subtropical jet stream results in a southward expansion of easterly trade winds (Garreaud et al., 2003) (Fig. 1). These favor the upslope transport of moisture

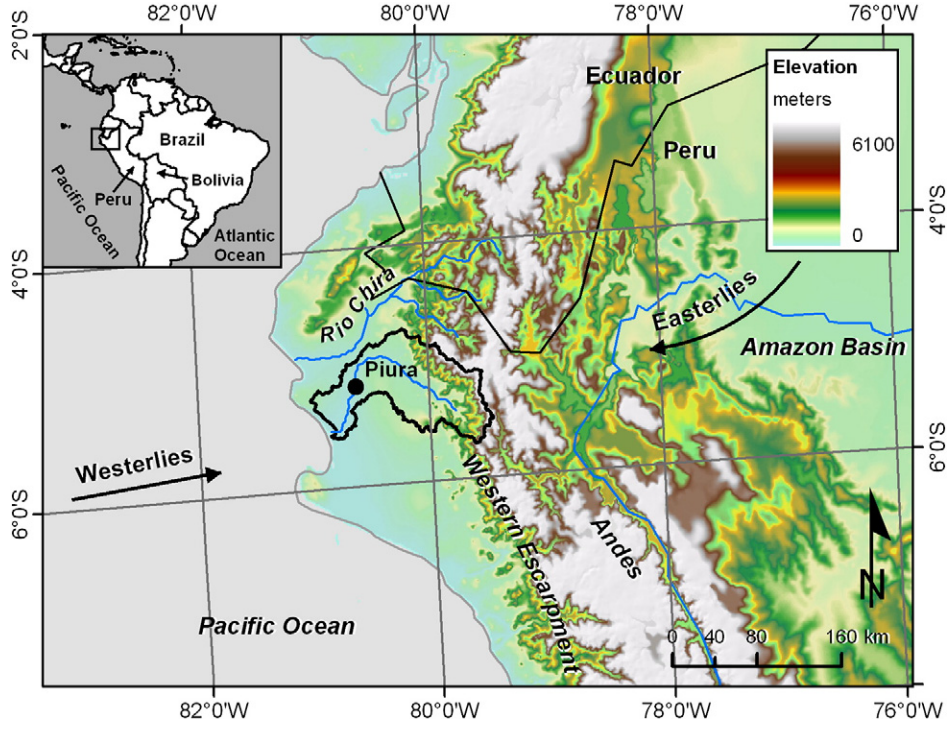

Fig. 1. Overview of the study area. The inset in the upper left corner shows the location within South America. The Rio Piura drains the Western Escarpment of the Andes and debouches into the Pacific Ocean.

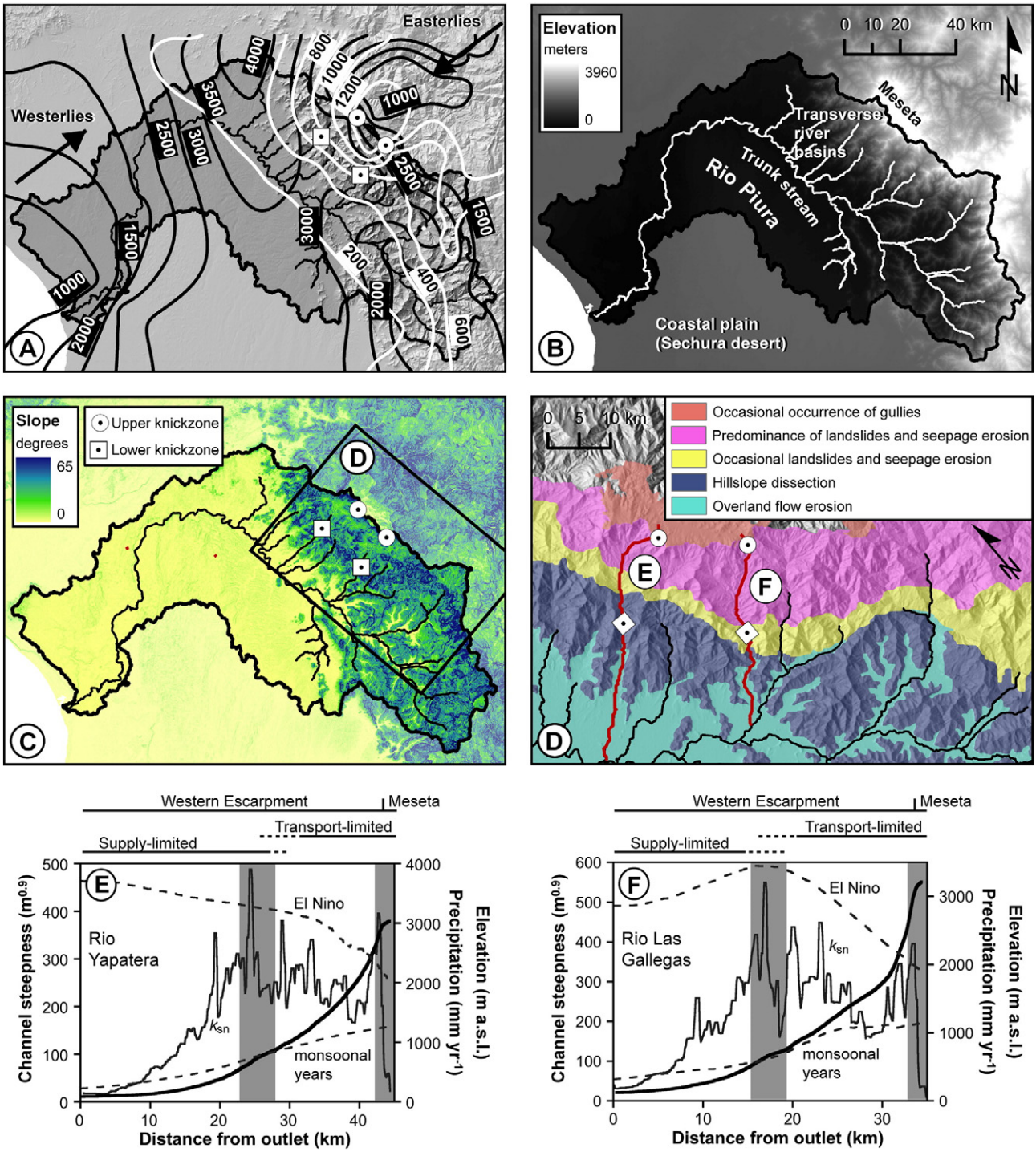

Fig. 2. Precipitation patterns, morphology, and sediment transport properties of the Rio Piura drainage system and longitudinal profiles of two transverse rivers within the basin. (A) Precipitation rates during monsoonal years (white lines) and precipitation rates during an El Niño year (here 1983 and 1998, black lines). Precipitation rates were measured by the hydrological service of Piura (Ministerio de Agricultura) and synthesized in Mettier et al. (2009). (B) Elevation from SRTM 90-m-resolution data. (C) Hillslope angle distribution within the catchment. The locations of the knickzones are illustrated by marking the upper boundary of the corresponding knickzone. Note the higher slope angles in the vicinity of the knickzones (see also Fig. 3C). (D) Varying sediment transport processes within the transverse catchments. Map taken from Mettier et al. (2009). (E) Channel steepness (grey line) and precipitation rates (dashed lines) along the Rio Yapatera. The lower knickzone (grey shaded) is located ca. 25 km, and the upper knickzone (grey shaded) ca. 43 km upstream of the river outlet. (F) Channel steepness and precipitation rates along the Rio Las Gallegas. The lower knickzone is located ca. 17 km, and the upper knickzone ca. 33 km upstream of the river outlet.

from the Amazon basin to the high Andes, resulting in convective rainfall at high elevations where the headwaters of the investigated rivers are situated (Garreaud, 1999). During austral winter from March to November, the ITCZ and the subtropical jet stream are located farther north, and a dry westerly wind aloft prevails (Fig. 1), hindering the upslope moisture transport from the Amazon basin. In the Rio Piura catchment, the direct consequence of these annual fluctuations is a decreasing amount of precipitation from ca. 1300 mm y^{-1} on the Meseta where the channel headwaters are located, to zero in the Sechura desert and at the Pacific coast (Fig. 2A) (Peru Ministerio de Agricultura; Mettier et al., 2009). We use the precipitation data reported in Mettier et al. (2009) in preference to the 9-year averaged

precipitation rate of Bookhagen and Strecker (2008) as the former are based on 25 years of local rainfall measurements and separate El Niño and normal years. These two datasets differ only in absolute magnitude, with the rates from Bookhagen and Strecker (2008) varying from ~500–100 mm y^{-1} over the same area.

Every 2–10 years in late December, the northern boundary of the cold Peru Current shifts farther south and the high pressure zone along the coast becomes weaker, marking the onset of an El Niño event. The effects are episodes of high but varying precipitation intensities. This was especially the case during the very strong (Quinn et al., 1987) 1982/83 and 1997/98 El Niño events. Particularly during the 1997/98 event, a total of up to 4000 mm cumulative rainfall was measured in the Sechura desert between December and June (Fig. 2A) (Mettier et al., 2009). Toward the east, the El Niño-related precipitation decreases with increasing elevation (Fig. 2A) such that on the Meseta, the difference between the total precipitation delivered during El Niño events and normal years becomes minimal (Mettier et al., 2009; Fig. 2A). Hence, El Niño episodes are characterized by anomalies in the precipitation pattern, with easterly and westerly sources and gradients, particularly in the lower segments of the Western Escarpment.

At the Peruvian coast, El Niño flooding events are documented to have started, or become more intense, at 5000–5800 cal BP (Rollins et al., 1986). In particular, Rodbell et al. (1999) reconstructed the periodicity of debris-flow deposition and found a progressive increase in frequency from ca. 15 years between 15,000–7000 years BP, to the modern 2 to 8.5 years at ca. 5000 calendar years BP.

Similarly, Quinn (1992) and Quinn et al. (1987)] documented an increase in El Niño recurrence intervals to modern ranges, but at a later time (i.e., at ca. 3000 cal BP; Sandweiss et al. (2001). Before 5800 cal BP, Rollins et al. (1986) suggest seasonal precipitation on the Peruvian coast and a lack of El Niño-like variability for some millennia. The spatial distribution and amplitude of beach ridges at river mouths (e.g., north of the Rio Piura outlet) support these assumptions (Rogers et al., 2004). Also, cultural changes on the Peruvian coast were considered to have occurred contemporaneously with these climatic transitions (Sandweiss, 2003). Other authors, however, proposed an arid climate similar to the modern one with intermittent warm-water incursions and catastrophic flooding events for at least the past 40,000 years or longer (Wells and Noller, 1997).

2.2. Geomorphology

The Rio Piura system drains a 10,000-km^2 area that is made up of ca. 50 km^2 transverse basins and an axial trunk system (Fig. 2B). The transverse rivers are sourced on the Meseta at >3000 m asl and drain the Western Escarpment of the Andes (Fig. 2B). These streams debouch into the Rio Piura trunk stream at ca. 200 m asl, which then crosses the Sechura desert and flows into the Pacific Ocean (Fig. 2B).

The transverse rivers of the Rio Piura have been divided into different geomorphologic segments with contrasting morphometric properties and sediment transport processes (Schneider et al., 2008; Mettier et al., 2009). On the Meseta, hillslope interfluves are mantled by a >5-m-thick regolith cover with convex landforms and nearly constant curvatures. In these soil-mantled landscapes, the maximal depth of hillslope erosion is limited to the regolith–bedrock interface. Sediment transport occurs here either by soil creep as indicated by the smooth curvature of the hillslopes, or by debris flows in gullies (Mettier et al., 2009) (Figs. 2D, 3A). The Western Escarpment is defined by a distinct upper limit, which we refer to as the upper knickzone (Fig. 2C). The topographic expression of this upper knickzone is as amphitheater-shaped escarpments with diameters of ~10-km width terminating each transverse river valley (Schneider et al., 2008). Garcia and Hérail (2005) and Schildgen et al. (2007) proposed that the knickzones at these elevations were initially formed in response to an enhanced surface uplift ca. 9–10 Ma ago. Hillslopes in this knickzone region are up to 60° steep and host abundant shallow landslides that transport the >3-m-thick regolith cover toward the channel network (Figs. 2C, 3B). The channel network consists of mixed bedrock–alluvial channels that are deeply incised into the landscape (Schneider et al., 2008). Mettier et al. (2009) used these geomorphic features to infer a transport-limited regime in the channels of these upper river segments (Fig. 2E, F). In the lowermost section, hillslopes are up to 35° steep (Fig. 2B), dissected by a network of debris-flow bedrock channels, and regolith cover is sparse (Fig. 3C) (Mettier et al., 2009), suggesting a supply-limited channel transport regime in these reaches (Fig. 2E, F). This also implies that, in contrast to the situation farther south (e.g., Pisco valley, Steffen et al., 2009), sediment storage en route is not significant since fill and cut-terraces are nearly absent. Further supporting evidence for the direct evacuation of sediment is the occurrence of smooth hillslopes with continuously increasing dip angles (e.g. Mettier et al., 2009). Interestingly, the upper transport-limited and the lower supply-limited river reaches are separated by a second knickzone in the stream-long profiles at lower elevations, referred to as the lower knickzone in this paper (Fig. 2B).

2.3. Geology

The western continental margin of northern South America is characterized by the active subduction of the Farallón–Nazca oceanic plate beneath the South American continental plate (Jaillard et al., 2000). Collision and arc magmatism started in the Early Jurassic with the onset of uplift of the Andean range 30 to 25 Ma ago (Isacks, 1988). The Andes of northern Peru and southern Ecuador formed by successive block accretions (e.g., Mourier et al., 1988).

In the study area, the bedrock on the Meseta comprises Cretaceous sediments (sandstones and cherts) and pyroclastic andesites (Reyes and Caldas, 1987). Farther downstream on the Western Escarpment, the bedrock is made up of the Cretaceous Coastal Batholith (granitic to dioritic rocks) that intruded into the Cretaceous sediments. The catchment areas of the Rio Yapatera and Rio Las Gallegas therefore consist of lithologies containing abundant quartz suitable for ^{10}Be analysis (Fig. 4). The coastal plain, forming the lowermost segment of the analyzed catchment, comprises mainly Quaternary fluvial, alluvial, and eolian deposits (Cobbing et al., 1981) underlain by Pliocene–Pleistocene shallow-marine sediments. These crop out at the coast and form uplifted marine terraces (Pedoja et al., 2006).

3. Methods

3.1. Morphometrics

Knickzones were identified on the stream-long profiles and confirmed by variations in channel steepness and concavity. The data were extracted from Shuttle Radar Topography Mission (SRTM) 90-m-resolution data (Farr et al., 2007) using the methods of Wobus et al. (2006). Under the assumption of similar lithologies and uplift rates, spatial patterns of channel steepness are indicators of relative stream power variations (e.g., Whipple, 2004; Safran et al., 2005; Korup, 2006). The steepness index relates channel gradients to the upstream size of catchments according to (e.g., Hack, 1973; Flint, 1974):

$$S = k_s A^{-\theta} \quad (1)$$

where k_s and θ are referred to as the steepness and the concavity index, respectively. In graded streams, channel concavity is a function of precipitation, where high annual rainfall and steeper precipitation gradients lead to more concave streams (Roe et al., 2002; Zaprowski et al., 2005). The channel steepness index is more directly related to the efficiency of channel erosion (e.g Safran et al., 2005). Accordingly, we

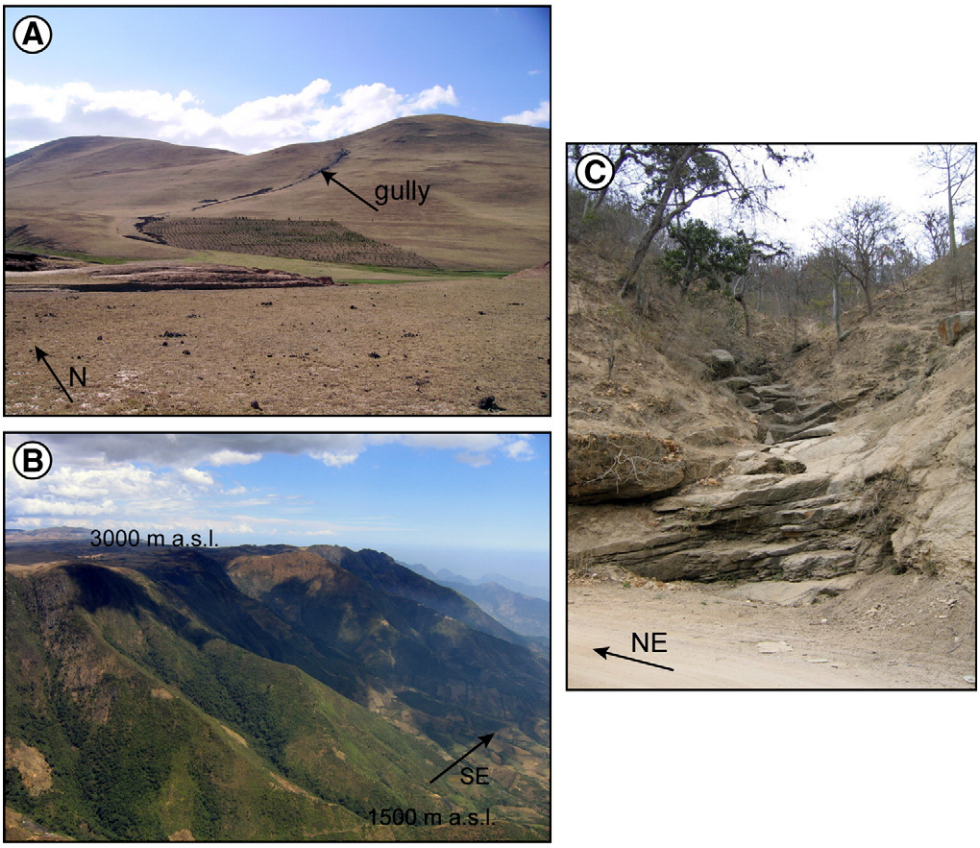

Fig. 3. Photographs taken within the Rio Piura catchment. (A) Landscape on the Meseta above the upper knickzone. (B) The upper knickzone region in the Rio Yapatera catchment. (C) Bedrock debris-flow channel in the lowermost part of the Rio Yapatera catchment.

calculated concavity of channel reaches and estimated k_{sn} values – k_s normalized to a reference concavity index of 0.45, a typical value for rivers in active mountain ranges and necessary for comparison – of the fluvial river network within the Rio Piura catchment (see Wobus et al. (2006) for methodological details). Values of k_{sn} were calculated by performing power-law regression on segments of S and A plots (Wobus

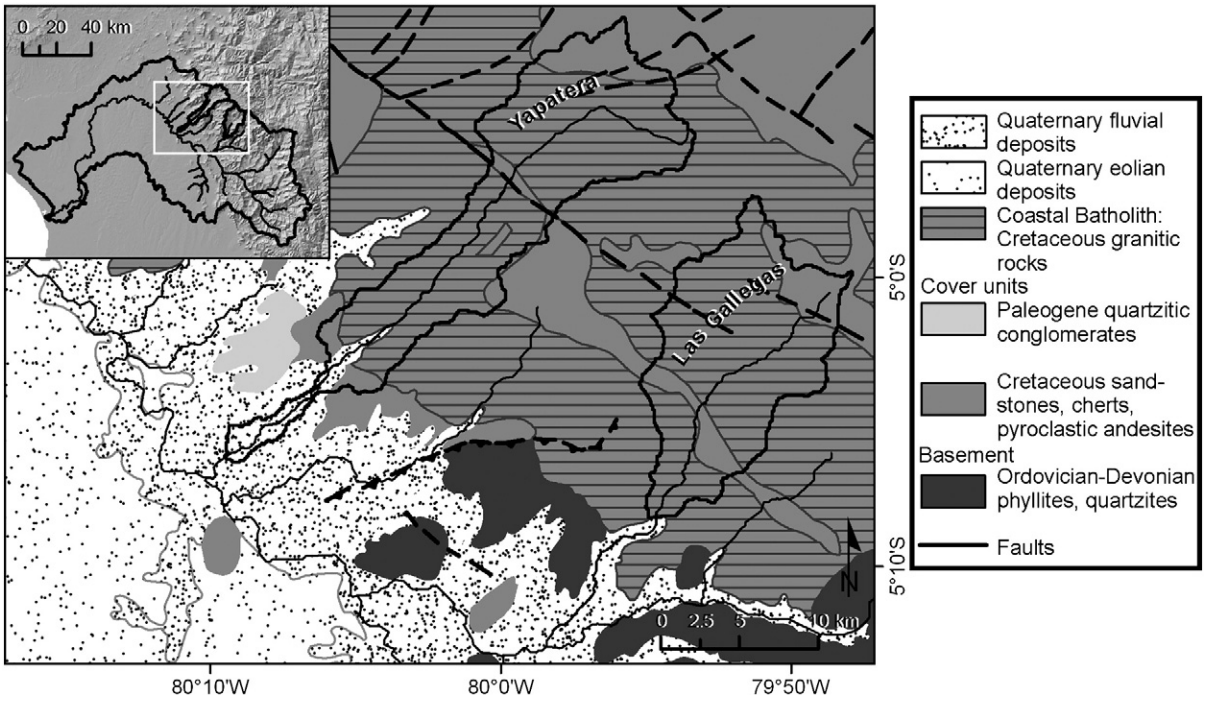

Fig. 4. Geologic architecture of the Rio Yapatera and Rio Las Gallegas basins. The inset in the upper left corner shows their position within the Rio Piura catchment. Geological map is taken from Reyes and Caldas (1987).

et al., 2006) for basins >1 km^2, i.e., basins that consist of stream-flow-dominated fluvial channels (e.g., Whipple, 2004).

3.2. Cosmogenic nuclides

The samples for ^{10}Be analysis were taken from sandbars in the active channels. The sample sites were selected to cover all geomorphologic and climatic domains along the river courses. In the Rio Piura catchment, a total of 14 samples were collected consecutively downstream along the main rivers, and 12 samples were taken in transverse tributary channels (Fig. 5; Table 1). In addition, 12 samples were taken in two depth profiles located within the Rio Yapatera catchment (Fig. 5). ^{10}Be concentrations estimated on depth profiles are anticipated to yield information about hillslope-scale denudation rates (Kober et al., 2007).

After sieving to the 0.4–1 mm grain size fraction, a purified quartz mineral separate was produced by selective chemical dissolution using 5% hydrofluoric acid (after Kohl and Nishiizumi, 1992). The hydrofluoric acid treatment was repeated several times to remove atmospheric ^{10}Be, and residual magnetic grains were removed using a Frantz Magnetic Barrier Separator. After dissolution of the clean quartz separate in concentrated hydrofluoric acid, ion exchange column separation (Aldahan and Possnert, 1998) was performed. The recovered Be-hydroxide was converted to BeO and mixed with Nb for accelerator mass spectrometry using a Pelletron (NEC) machine and the AMS system at the Uppsala University Tandem Laboratory. The machine ^{10}Be/^{9}Be background was at $(4–6)\times10^{-15}$, and the measured blank ratios were at $(1–3)\times10^{-14}$. The measured ^{10}Be/^{9}Be ratios were normalized to the NIST SRM 4325 standard with a nominal ratio of 3.03×10^{-11} (Nishiizumi et al., 2007), based on a ^{10}Be half-life of 1.51 ± 0.06 My (Hofmann et al., 1987). We also use this half-life, instead of the newer 1.39 ± 0.1 My (Chmeleff et al., 2010) for calculating denudation rates for consistency in the calculations. Note, however, that the choice of half-life makes little difference in the final denudation rates as the erosion timescales here are from ~10^4–10^5.

The ^{10}Be concentrations were used to calculate catchment-wide denudation rates (Brown et al., 1995; Bierman and Steig, 1996; Granger et al., 1996). Because topography reduces the incoming cosmic ray flux, a sample catchment specific shielding factor was calculated following Norton and Vanacker (2009). Sample catchments were delineated according to the sample location in 90-m-resolution SRTM data. Scaling of the sea-level, high latitude ^{10}Be production rate of 5.1 atoms g^{-1}_{qtz} y^{-1} to altitude and latitude was performed on a cell-by-cell basis by applying a modification of the scaling laws of Stone (2000) to the spallation (fast neutrons) and slow muon capture production pathways and then averaged over the basin. Production by fast muon reactions was not scaled to altitude and latitude. The ^{10}Be concentrations were converted into denudation rates (Granger et al., 1996; Granger and Smith, 2000) by assuming that all eroding areas within the catchment contributed to the mixed sediment sample in proportion to their erosion rates (e.g., von Blanckenburg, 2005). We assumed a bedrock density of 2.7 g cm^{-3}. No corrections for uplift or paleomagnetic field variations were applied. Modeled ^{10}Be concentrations of the in situ depth profiles were calculated using the production rates and absorption laws of Granger and Smith (2000). Analytical and altitude estimate uncertainties of denudation rates (Table 1, internal uncertainty) and further systematic uncertainties in production rate and denudation rate estimates (Table 1, total uncertainty) were propagated by Monte Carlo simulation, generally assuming that the error terms are not correlated and Gaussian distributed. Internal uncertainties reported in Table 1 are appropriate for intersample comparison, while total uncertainties are relevant for intermethod comparisons.

4. Results

The river longitudinal profiles of the Rio Yapatera (Fig. 2E) and the Rio Las Gallegas (Fig. 2F) display a similar morphometric pattern, with identifiable upper and lower knickzones. The lower knickzone spatially coincides with the regions where precipitation rates during El Niño events reach a maximum, particularly in the Rio Las Gallegas catchment (Fig. 2F). Peak k_{sn} values correlate with the upper knickzones and with a broad zone around the lower knickzone (Figs. 2E, F, 6). Note that while the upper knickzone is potentially related to lithology, the

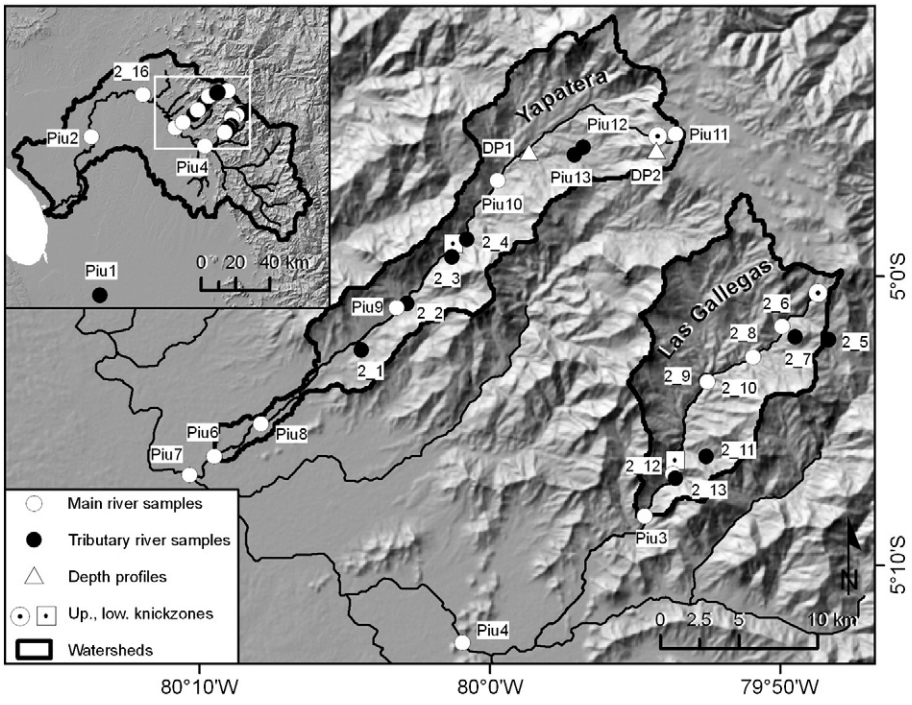

Fig. 5. Location of the sampling sites. In the upper left corner, the entire Rio Piura catchment is shown. The white rectangle shows the extent of the more detailed map of the Rio Yapatera and Rio Las Gallegas catchments.

Table 1
Cosmogenic nuclide-derived denudation rates estimated within the Rio Piura catchment in northwestern Peru.

Sample	Latitude[b] (dd)	Longitude[b] (dd)	Depth (cm)	Area (km^2)	Mean altitude (m)	Shielding factor[c]	Product rate[d] (atoms g^{-1}_{qtz} $year^{-1}$)	^{10}Be concentration[e] (atoms g^{-1}_{qtz})*10^4	Denudation rate[f] (mm ky^{-1})	Internal uncertainty[g] (mm ky^{-1})	Total uncertainty[h] (mm ky^{-1})	App. Age [i] (k y)
Main river samples[a]												
Yapatera river												
Piu11	−4.9181	−79.8939	–	1.1	3084	0.992	33.15	223.3 ± 5.4	8.86	0.51	1.26	68
Piu10	−4.9451	−79.9960	–	98.4	2054	0.908	19.69	7.32 ± 0.56	157	14	24	4
Piu9	−5.0183	−80.0537	–	150.7	1708	0.905	16.41	6.24 ± 0.52	155	16	24	4
Piu8	−5.0856	−80.1315	–	184.9	1461	0.914	14.54	5.91 ± 0.53	148	16	24	4
Piu6	−5.1041	−80.1583	–	191.0	1418	0.917	14.25	7.92 ± 0.39	107.6	7.6	15	6
Las Gallegas river												
2_6	−5.0288	−79.8326	–	12.3	2535	0.856	25.33	34.9 ± 4.2	39.6	5.4	7.3	15
2_8	−5.0465	−79.8493	–	27.2	2191	0.895	20.96	6.0 ± 1.0	206	40	48	3
2_10	−5.0608	−79.8752	–	51.2	2006	0.907	18.90	3.68 ± 0.43	304	39	55	2
2_12	−5.1138	−79.8952	–	137.1	1827	0.911	17.23	7.0 ± 1.2	150	30	35	4
Piu3	−5.1382	−79.9111	–	148.1	1754	0.908	16.61	5.42 ± 0.37	181	16	27	3
After confluence with the trunk stream of the Piura river												
Piu4	−5.2114	−80.0157	–	2916.7	1117	0.917	11.82	15.2 ± 1.5	47.2	5.4	7.9	13
Piu7	−5.1150	−80.1725	–	4653.8	877	0.938	10.19	8.2 ± 1.1	79	11	15	8
2_16	−4.9380	−80.3436	–	6380.1	718	0.950	9.09	28.2 ± 4.0	20.4	3.3	4.2	29
Piu2	−5.1617	−80.6149	–	7478.3	630	0.957	8.52	19.1 ± 1.4	28.5	2.6	4.4	21
Tributary river samples[a]												
Yapatera tributaries												
Piu13	−4.9299	−79.9517	–	7.1	2355	0.876	22.96	7.5 ± 1.5	180	43	49	3
Piu12	−4.9257	−79.9466	–	3.4	2147	0.906	20.03	5.84 ± 0.39	200	17	30	3
2_4	−4.9787	−80.0136	–	2.6	1319	0.878	12.03	7.34 ± 0.71	96	11	16	6
2_3	−4.9888	−80.0219	–	1.3	1172	0.829	10.93	3.46 ± 0.48	178	28	35	3
2_2	−5.0158	−80.0478	–	10.5	1042	0.886	10.16	4.77 ± 0.49	127	15	21	5
2_1	−5.0427	−80.0738	–	1.1	468	0.932	6.72	6.21 ± 0.49	69.8	6.7	10.6	9
Las Gallegas tributaries												
2_5	−5.0364	−79.8058	–	3.3	2717	0.907	27.54	25.5 ± 1.8	62.0	5.5	9.6	10
2_7	−5.0347	−79.8250	–	0.2	2134	0.905	19.72	5.8 ± 1.2	208	53	59	3
2_9	−5.0600	−79.8761	–	44.1	2127	0.924	20.32	8.18 ± 0.62	148	14	23	4
2_11	−5.1037	−79.8760	–	6.8	1501	0.907	13.55	19.8 ± 1.3	40.4	3.5	6.1	15
2_13	−5.1163	−79.8936	–	3.4	1127	0.813	10.65	21.9 ± 1.2	25.7	1.9	3.7	23
Sechura desert												
Piu1	−5.9992	−80.5682	–	40.1	9	1.000	4.86	37.3 ± 2.3	8.56	0.73	1.32	70
In situ depth profile samples												
DP1_2	−4.9287	−79.9779	30	–	1336	–	11.67[§]	6.90 ± 0.55	–	–	–	–
DP1_3	−4.9287	−79.9779	60	–	1336	–	11.67[§]	5.50 ± 0.45	–	–	–	–
DP1_4	−4.9287	−79.9779	100	–	1336	–	11.67[§]	15.90 ± 0.85	–	–	–	–
DP1_5	−4.9287	−79.9779	150	–	1336	–	11.67[§]	4.36 ± 0.43	–	–	–	–
DP1_6	−4.9287	−79.9779	200	–	1336	–	11.67[§]	4.49 ± 0.42	–	–	–	–
DP1_7	−4.9287	−79.9779	300	–	1336	–	11.67[§]	6.63 ± 0.52	–	–	–	–
DP2_2	−4.9275	−79.9050	30	–	1336	–	32.16[§]	29.14 ± 0.91	–	–	–	–
DP2_3	−4.9275	−79.9050	60	–	3014	–	32.16[§]	4.00 ± 0.60	–	–	–	–
DP2_4	−4.9275	−79.9050	100	–	3014	–	32.16[§]	18.5 ± 1.1	–	–	–	–
DP2_5	−4.9275	−79.9050	150	–	3014	–	32.16[§]	9.70 ± 0.90	–	–	–	–
DP2_6	−4.9275	−79.9050	200	–	3014	–	32.16[§]	6.40 ± 0.60	–	–	–	–
DP2_7	−4.9275	−79.9050	300	–	3014	–	32.16[§]	5.10 ± 0.60	–	–	–	–

[a] Samples are ordered downstream along the particular river course.
[b] Coordinates are in WGS84.
[c] Catchment-wide skyline shielding factor, calculated following the approach of Norton and Vanacker (2009).
[d] Scaling to altitude and latitude was done by using a modification of the scaling laws of Stone (2000).
[e] ^{10}Be concentration with 1σ-analytical error.
[f] Long-term denudation rates (Granger et al., 1996; Granger and Smith, 2000) calculated with a bedrock density of 2.7 g cm^{-3}.
[g] The listed internal uncertainties of the corresponding denudation rates are propagated from analytical uncertainties (specific for each sample) and altitude estimate uncertainties (stdv = 5%) and are relevant for intersample comparisons.
[h] The listed total uncertainties (external uncertainties) are relevant for intermethod comparisons and for comparison with cosmogenic nuclide-based studies at other locations. They were propagated from analytical uncertainties (specific for each sample), altitude estimate uncertainties (stdv = 5%), uncertainties of the sea-level, high latitude ^{10}Be production rate (stdv = 6%), the scaling factors (stdv = 10%), the attenuation lengths (stdv = 6%) and the ^{10}Be half-life (stdv = 4%).
[i] The apparent age approximates the integration timescale of the method. It corresponds to the time required to erode the landscape by one attenuation length scale of the cosmogenic radiation (here only for spallation, ~0.6 m of material).
[§] Surface production rate.

spatial distribution of k_{sn} values, especially around the lower knickzones, is neither determined by the underlying bedrock lithology, nor related to faults (Fig. 6). Channel concavities are likewise enhanced beneath both the upper and lower knickzones, with values as high as 5.4 (Fig. 7C, D).

The ^{10}Be-derived apparent catchment-wide denudation rates of the main and tributary river samples reveal an overall decreasing trend in the downstream direction toward the coast (Fig. 7). In the Rio Yapatera catchment, denudation rates in the trunk stream are 8.86 ± 0.51 mm ky^{-1} on the Meseta (Fig. 7A). Beneath the upper knickzone, denudation rates are enhanced, decreasing from 157 ± 14 mm ky^{-1} to 107.6 ± 7.6 mm ky^{-1} before the Rio Yapatera debouches into the Rio Piura (Fig. 7A). Calculated denudation rates of the tributary river samples decrease more rapidly over the same distance, from 200 ±

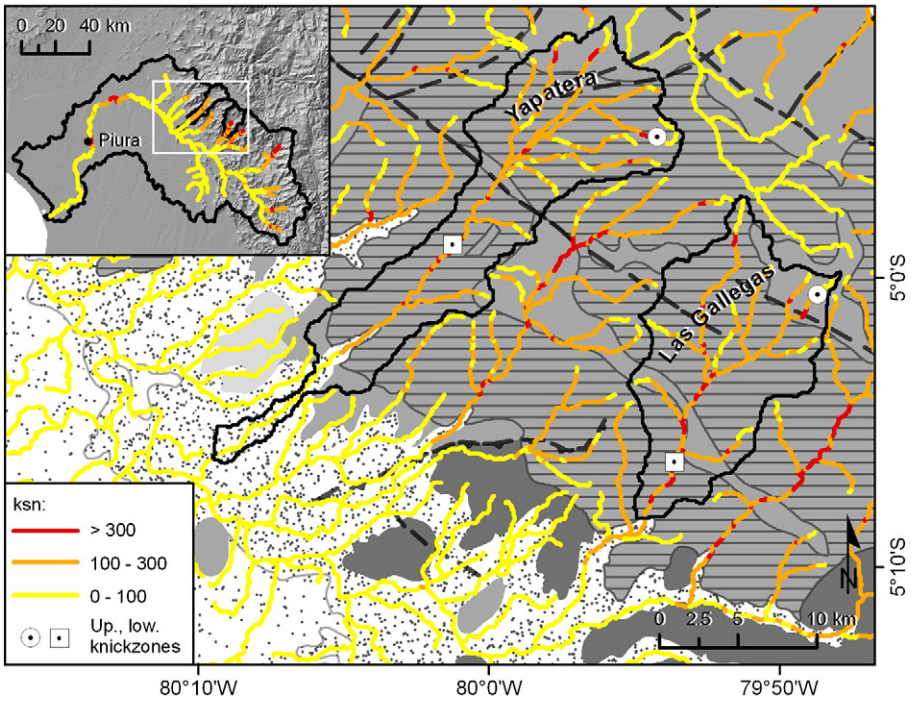

Fig. 6. Spatial pattern of normalized channel steepness index values (k_{sn}) and knickzones within the investigated area and their spatial relation to bedrock lithology and faults. The streams are color-coded by k_{sn} values. The legend for the geological base map is presented in Fig. 4. Faults are shown with a black-dashed line.

17 mm ky^{-1} to 69.8 ± 6.7 mm ky^{-1} (Fig. 7A). Denudation rates estimated within the Rio Las Gallegas catchment display an identical pattern. In particular, trunk stream denudation rates increase from 39.6 ± 5.4 mm ky^{-1} on the Meseta to 304 ± 39 mm ky^{-1} below the upper knickzone (Fig. 7B). Farther downstream beneath the lower knickzone, trunk stream denudation rates decrease to 150 ± 30 mm ky^{-1} (Fig. 7B). Similar to the denudation rate pattern of the Rio Yapatera, denudation rates of the tributary catchments decrease more rapidly, from 208 ± 53 mm ky^{-1} to 25.7 ± 1.9 mm ky^{-1} (Fig. 7B), than those of the trunk stream. Furthermore, denudation rates of both transverse catchments mirror the normal easterly precipitation pattern, decreasing in a downstream direction (Fig. 7).

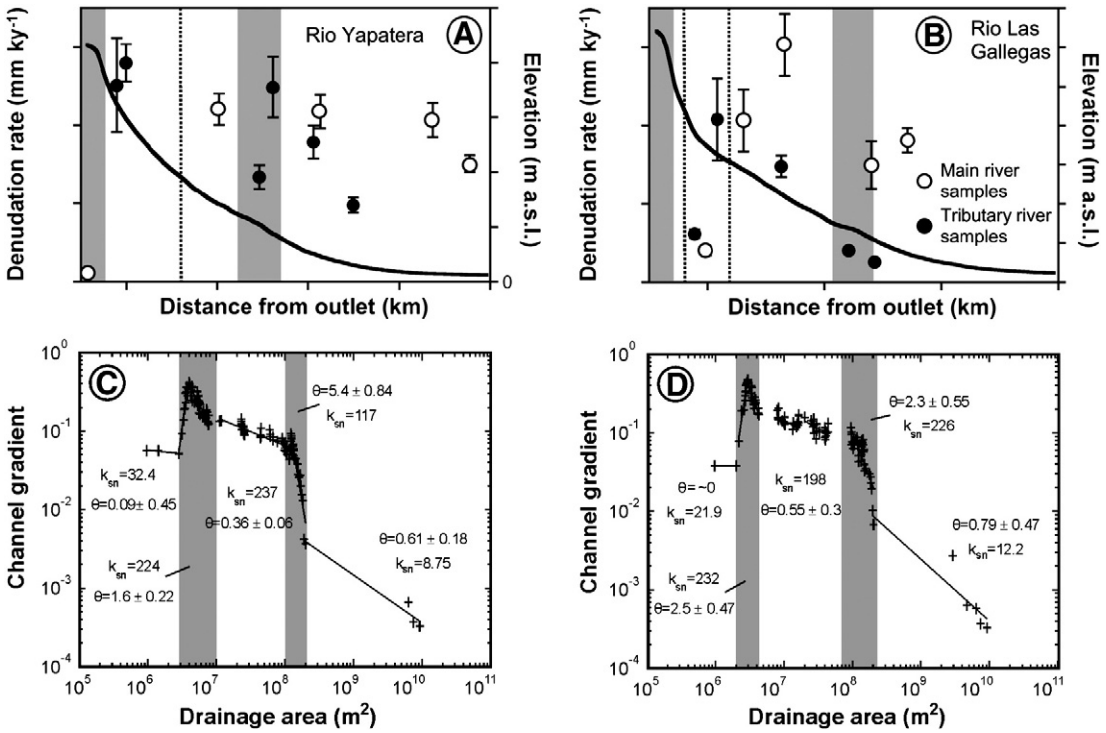

Fig. 7. Stream-long profiles of the (A) Rio Yapatera and the (B) Rio Las Gallegas together with apparent catchment-wide denudation rates (mean value ± 1 standard deviation). In both diagrams, the grey shaded areas represent the locations of the upper and lower knickzones. Slope-area plots for the (C) Rio Yapatera and the (D) Rio Las Gallegas. Again, the grey shaded areas represent the knickzones (here associated with high steepness values and high concavities). Fault traces are shown with a dashed black line.

On the coastal plain, apparent catchment-wide denudation rates range between 79 ± 11 mm ky^{-1} and 8.56 ± 0.73 mm ky^{-1} (Table 1).

The two regolith profiles exhibit differing patterns of ^{10}Be concentration with depth. Profile DP2 (Fig. 8A) shows the expected exponential decrease for a non-disturbed steadily eroding surface (e.g., Granger and Riebe, 2007). We treat the sample at 0.6 m depth as an outlier because its ^{10}Be concentration does not fit the general decreasing trend. The estimated ^{10}Be concentrations of this profile fit best to a modeled steady-state profile with corresponding denudation rates of 10 mm ky^{-1} to ca. 50 mm ky^{-1} (Fig. 8A). In contrast, profile DP1 (Fig. 8B), which is located farther downstream, lacks a clear exponential decrease in 10Be concentrations, and more closely resembles a mixed eroding surface (Granger and Riebe, 2007). We are, however, unable to determine whether post-mixing erosion has taken place. Therefore, according to Granger and Riebe (2007), the nuclide concentrations could represent either the average nuclide concentration of the entire mixed zone (no erosion) or that of the surface (steady-state erosion). As a result, modeled erosion rates could be between ~70 mm ky^{-1} and 140 mm ky^{-1}. The calculation excludes the ^{10}Be concentration estimated at 1 m depth, which might represent the surface material which has been moved down.

5. Discussion and conclusion

5.1. Mechanisms of landscape denudation within the Rio Piura catchment

The normalized steepness index k_{sn} has been used to identify zones of enhanced erosion, or specifically enhanced river incision (e.g., Safran et al., 2005). A plot of the ^{10}Be-derived catchment-wide denudation rates versus mean k_{sn}, calculated from all stream k_{sn} values within each sample catchment, shows a positive correlation between denudation rates and k_{sn} values ($R^2 = 0.59$), albeit with large variance (Fig. 9). As the lower channel segments are supply limited, this positive correlation may indicate a control by fluvial, relief-generating processes on landscape evolution in the lower reaches of the Rio Piura catchment (Whipple, 2004). The spatial correspondence of the maximum k_{sn} values in the upper and lower knickzones with high denudation rates (particularly for the tributary catchments around the knickzone reaches of the Rio Yapatera) additionally supports this interpretation (Figs. 2E, F, 7). Alternatively, k_{sn} patterns (Fig. 6) can also be interpreted as reflecting a tectonic control as shown for the Bolivian Andes by Safran et al. (2005), or be associated with landslides or lithologic changes (e.g. Korup, 2006). We cannot exclude these possibilites but emphasize that peak k_{sn} values do not spatially correlate with known faults (Fig. 6). Furthermore, only the upper knickzone is associated with landslides and a change in lithology (as may be expected on a retreating escarpment). The lower knickzone is, however, not associated with any changes in tectonics, landslide frequency, or lithology. Therefore, we favor a geomorphic control on k_{sn} patterns in the Rio Piura.

Both the upper and lower knickzones also exhibit high stream concavities. The upper knickzone on the Western Escarpment erodes headward by parallel retreat (Schlunegger et al., 2006), maintaining the form of the longitudinal profile over the My timescale of these gorges. The initial formation and subsequent headward erosion of the upper knickzone were in response to a Late Miocene phase of surface uplift (Schlunegger et al., 2006; Schildgen et al., 2007). Because this erosion is progressing through a headward retreat, high channel steepnesses and concavities should also be maintained below the escarpment edge, as observed for the upper knickzone here. An equivalent of the lower knickzone, however, has not been documented elsewhere on the Western Escarpment, and is related to neither lithologic changes nor fault locations. This knickzone does, however, spatially coincide with maximum relative El Nino influence (e.g. where El Nino precipitation is still high, and orographic monsoonal precipitation is already low). This hints towards a climatic forcing for the high concavities of the lower knickzone as suggested by theory (Roe et al., 2002). Precipitation-driven high concavities also point towards a fluvial control on erosion and sediment evacuation.

5.2. Transient state of landscape development

Tributary catchments in the area around the lower knickzone and farther downstream display lower denudation rates than those estimated for the Rio Yapatera and Rio Las Gallegas trunk channels

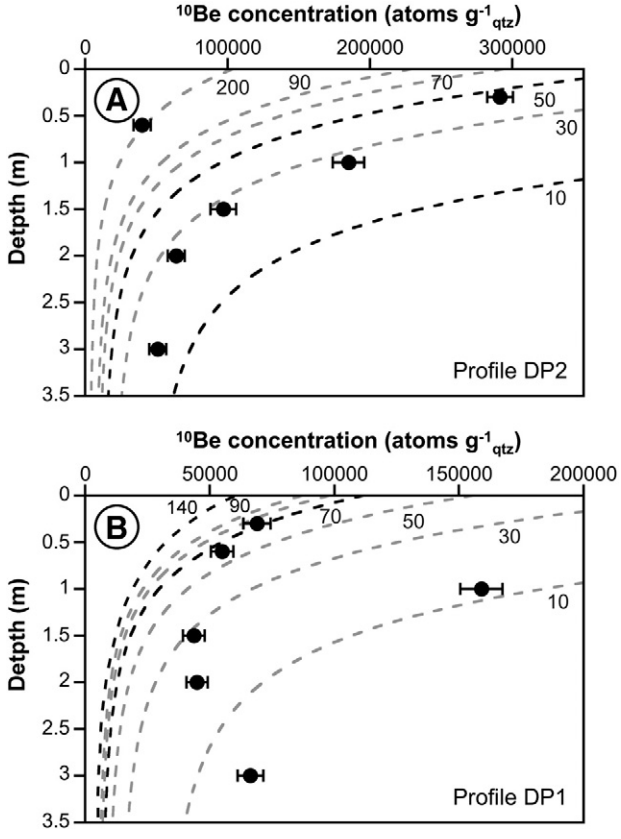

Fig. 8. Plot of estimated ^{10}Be concentrations versus depth for the two depth profiles established in the Rio Yapatera catchment. The dashed lines indicate modeled steady-state ^{10}Be concentrations for different denudation rates, of which the black colored are 10 mm ky^{-1} to 50 mm ky^{-1}, and 70 mm ky^{-1} to 140 mm ky^{-1}, for DP2 and DP1 respectively. The black dots are measured ^{10}Be concentrations ± 1 standard deviation. (A) Profile DP2. (B) Profile DP1.

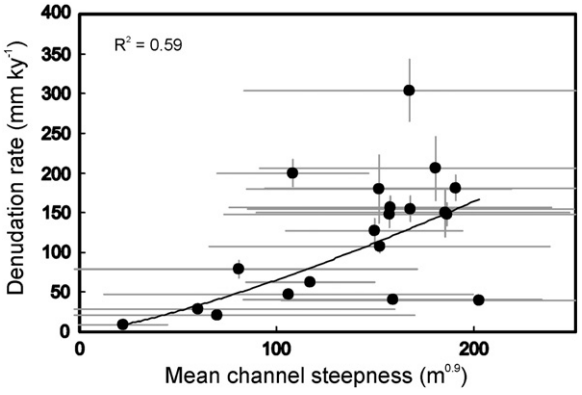

Fig. 9. Catchment-wide denudation rates of all ^{10}Be samples (mean value ± 1-sigma error) plotted against mean normalized steepness indices (mean k_{sn} ± 1-sigma variance) for each catchment.

(Fig. 7). The higher erosion rates in the corresponding reaches of the trunk channels suggest a transient state in landscape evolution, where incision of the trunk stream has not yet fully propagated up the hillslopes and into the bordering tributary catchments. Supporting evidence for this interpretation are ^{10}Be concentrations measured in regolith profiles, DP1 and DP2, that yield lower hillslope-scale denudation rates than the apparent catchment-wide denudation rates estimated for the surrounding basins (Piu 11, 12, and 13). This further implies that the landscape is in a stage of local relief growth, where channels are incising into the more slowly eroding hillslopes.

The downstream decreasing trends of denudation rates estimated within the trunk and tributaries support the conclusions of Kober et al. (2009) for the Rio Lluta in northern Chile that main channels are eroding more rapidly than small tributaries. In this scenario, low concentration sediment that is produced in the upper knickzone by the combined effects of landsliding and fluvial entrainment is transferred downstream and mixed with decreasing contribution from tributary catchments. This could take place either in cosmogenic steady state (e.g. a long-lived landscape), or as transient incision into the trunk channel. Either scenario would result in the observed denudation pattern where catchment-wide denudation rates of the trunk channels decrease downstream. A transient incision pulse (e.g. not in cosmogenic steady state) does not, however, explain the observed pattern of decreasing tributary catchment denudation rates over the same distance. While we cannot discard either possibility, we prefer an interpretation where the denudation rate pattern results from a combination of (i) transient incision of the channel network and (ii) downstream decreasing trends of denudation rates on bordering hillslopes. This interpretation is consistent with the general decreasing trend of denudation rates for successively smaller scales upstream (trunk channels, tributary channels, hillslopes), indicating landscape transience and local relief growth. In addition, this interpretation also considers downstream mixing of material that has experienced successively lower denudation rates.

5.3. Climatic forcing on landscape erosion

The observation that denudation rates decrease together with decreasing easterly precipitation rates (Figs. 2E, F, 7) implies that the monsoonal climatic pattern has imprinted on erosion. This requires that the modern monsoonal precipitation pattern is a long-lived feature. Studies of Andean climate and tectonics do indeed suggest that the modern orographic barrier has been in place since 25–5 Ma (e.g. Ehlers and Poulsen, 2009). Furthermore, because the precipitation gradient in the study area is perpendicular to the orientation of the smaller scale tributary catchments, the precipitation gradient within each individual tributary catchment is minimal. Therefore, we consider the downvalley decreasing trend of denudation rates in tributary catchments to be largely controlled by the downstream decrease in precipitation brought by easterly winds. This scenario dominates during normal climatic periods. In contrast, we tentatively relate the transience and the growth of local relief (in response to trunk channel incision, see Section 5.2) to the influence of the westerly-wind precipitation during El Niño periods. In particular, the spatial coincidence between the lower knickzones in the stream-long profiles, the highest stream concavities, and the highest precipitation rates during El Niño events (Fig. 2) suggest that climate may be an important factor for long-profile geometries and channel incision (e.g., Zeilinger and Schlunegger, 2007). Indeed, as mentioned above and illustrated based on theoretical grounds (e.g., Roe et al., 2002), the channel reaches of highest concavities reflect the stream's response to the largest downstream precipitation gradient controlled here by El Niño events. The morphometric properties of a landscape are characterized by response times of tens to hundreds of thousands of years (e.g., Whipple and Tucker, 1999; Whipple, 2009). Therefore, assuming that these geomorphic features have formed in response to a climate forcing, e.g. El Niño, we consider this phenomenon as a long-lived feature (e.g., Wells and Noller, 1997).

A downstream increase in supply limits of sediment transport, as suggested by Mettier et al. (2009), implies a downstream decrease in the relative importance of sediment production on hillslopes versus sediment transport in channels. Also as described by the same authors, sediment transport in the channel network is mainly accomplished during El Niño events. Accordingly, the downstream decrease in the relative importance of hillslope sediment production versus channelized sediment transport may reflect the combined effect of a downstream increasing trend of channel network efficiency and a downstream decreasing trend of hillslope processes, including weathering. Because of the close correlation between easterly precipitation rates and tributary catchment denudation rates (Fig. 2), we envision that the monsoonal easterly precipitation controls transformation of bedrock into regolith by bedrock weathering, providing the sediment for transport during El Niño flooding events. The lower river segments, which are characterized by supply-limited channel transport conditions, then provide the geomorphologic (by the availability of a linked channel network) and climatic (by the combined influence of easterly and westerly precipitation) conditions to maximize sediment export. This is in contrast to the situation in the coastal plain where low relief, together with a lack of a linked channel network, is responsible for low denudation rates (around 9 mm ky^{-1}; Table 1), despite the high precipitation rates during an El Niño event.

5.4. Timescales of denudation and El Niño

The averaging timescales of the cosmogenic ^{10}Be-derived denudation rates of main and tributary river samples of the Rio Yapatera and Rio Las Gallegas, estimated in the catchment segments affected by El Niño events, are in the range of 3 to 9 ky with a mean-averaging timescale of 5 ky (Table 1). The onset of Holocene El Niño flooding events in northern Peru is the subject of ongoing discussions, with suggestions spanning from an onset around 5800 cal BP (e.g., Rollins et al., 1986) to El Niño events existing throughout the Holocene and beyond (Wells and Noller, 1997). However, Rein (2007) showed that in a Holocene perspective, the intensity of these early events is not exceptionally high. Other authors also propose weaker El Niño events before 5000 cal BP (Rodbell et al., 1999), and a subsequent intensification at 3000 cal BP. It is then possible that an increase in the recurrence intervals of El Niño events during the past 3000 years, or even earlier (Quinn et al., 1987; Quinn, 1992; Sandweiss et al., 2001) accelerated sediment transport and erosion in channels, which we use here to explain the higher erosion rates (low nuclide concentrations) in the trunk channels compared to the bordering hillslopes, and the inferred growth of the local relief. Certainly, the 3000–5000 years of precipitation change are shorter than the integration time of ^{10}Be, but are sufficiently long to be partially detected by this method. Accordingly, the effects of recent local relief growth due to the change in El Niño precipitation intensities and frequencies, as measured by ^{10}Be based denudation rates, are if anything, underestimated.

The inferred transience in the landscape and the related increase in the local relief can, therefore, be considered to be a response to an increase in the recurrence intervals of El Niño events on the Western Escarpment in northern Peru.

Acknowledgements

The help of H. Schneider and K. Ramseyer in the field is greatly appreciated. This research was supported by the Swiss National Science Foundation (grant no. 200020-121680/1).

References

Aldahan, A., Possnert, G., 1998. A high-resolution 10Be profile from deep sea sediment covering the last 70 ka: indication for globally synchronized environmental events. Quaternary Science Reviews 17 (11), 1023–1032.

Bierman, P., Steig, E.J., 1996. Estimating rates of denudation using cosmogenic isotope abundances in sediment. Earth Surface Processes and Landforms 21 (2), 125–139.

Bookhagen, B., Strecker, M.R., 2008. Orographic barriers, high-resolution TRMM rainfall, and relief variations along the eastern Andes. Geophysical Research Letters 35, L06403. doi:10.1029/2007GL032011.

Brown, E.T., Stallard, R.F., Larsen, M.C., Raisbeck, G.M., Yiou, F., 1995. Denudation rates determined from the accumulation of in situ-produced 10Be in the Luquillo Experimental Forest, Puerto Rico. Earth and Planetary Science Letters 129, 193–202.

Burbank, D.W., Blythe, A.E., Putkonen, J., Pratt-Sitaula, B., Gabet, E., Oskin, M., Barros, A., Ojha, T.P., 2003. Decoupling of erosion and precipitation in the Himalayas. Nature 426, 652–655.

Chmeleff, J., von Blanckenburg, F., Kossert, K., Jacob, D., 2010. Determination of the 10Be half-life by multicollector ICP-MS and liquid scintillation counting. Nuclear Instruments and Methods B 268, 192–199.

Cobbing, E.J., Pitcher, W.S., Wilson, J.J., Baldock, J.W., Taylor, W.P., McCourt, W., Snelling, N.J., 1981. The Geology of the Western Cordillera of Northern Perú. Memoir 5. Institute of Geological Sciences Overseas, London. 143 pp.

Cox, N.J., 1980. On the relationship between bedrock lowering and regolith thickness. Earth Surface Processes and Landforms 5, 271–274.

Dadson, S.J., Hovius, H., Chen, H., Brian Dade, W., Hsieh, M-L., Willett, S.D., Hu, J-C., Horng, M-J., Chen, M-C., Stark, C.P., Lague, D., Lin, J.C., 2003. Links between erosion, runoff variability and seismicity in the Taiwan orogen. Nature 426, 648–651.

Ehlers, T.A., Poulsen, C.J., 2009. Influence of Andean uplift on climate and paleoaltimetry estimates. Earth and Planetary Science Letters 281, 238–248. doi:10.1016/j.epsl.2009.02.026.

Farr, T.G., Rosen, P.A., Caro, E., Crippen, R., Duren, R., Hensley, S., Kobrick, M., Paller, M., Rodriguez, E., Roth, L., Seal, D., Shaffer, S., Shimada, J., Umland, J., Werner, M., Oskin, M., Burbank, D., Alsdorf, D., 2007. The Shuttle Radar Topography Mission. Reviews of Geophysics 45 (2), RG2004.

Flint, J.J., 1974. Stream gradient as a function of order, magnitude, and discharge. Water Resources Research 10 (5), 969–973.

Garcia, M., Hérail, G., 2005. Fault-related folding, drainage network evolution and valley incision during the Neogene in the Andean Precordillera of Northern Chile. Geomorphology 65 (3–4), 279–300.

Garreaud, R.D., 1999. Multiscale analysis of the summertime precipitation over the central Andes. Monthly Weather Review 127 (5), 901–921.

Garreaud, R., Vuille, M., Clement, A.C., 2003. The climate of the Altiplano: observed current conditions and mechanisms of past changes. Palaeogeography, Palaeoclimatology, Palaeoecology 194 (1–3), 5–22.

Granger, D.E., Riebe, C.S., 2007. Cosmogenic nuclides in weathering and erosion. In: Drever, J.I. (Ed.), Surface and Ground Water, Weathering, and Soils. : Treatise on Geochemistry, 5. Elsevier-Pergamon, Oxford, UK, pp. 1–43.

Granger, D.E., Smith, A.L., 2000. Dating buried sediments using radioactive decay and muogenic production of Al-26 and Be-10. Nuclear Instruments & Methods in Physics Research Section B: Beam Interactions with Materials and Atoms 172, 822–826.

Granger, D.E., Kirchner, J.W., Finkel, R., 1996. Spatially averaged long-term erosion rates measured from in situ-produced cosmogenic nuclides in alluvial sediment. Journal of Geology 104 (3), 249–257.

Hack, J.T., 1973. Stream profile analysis and stream-gradient index. U.S. Geological Survey Journal of Research 1 (4), 421–429.

Heimsath, A.M., Dietrich, W.E., Nishiizumi, K., Finkel, R.C., 1997. The soil production function and landscape equilibrium. Nature 388, 358–361.

Hofmann, H.J., Bonani, G., Suter, M., Wölfli, W., Zimmermann, D., von Gunten, H.R., 1987. 10Be: half-life and AMS-Standards. Nuclear Instruments & Methods in Physics Research Section B: Beam Interactions with Materials and Atoms 29 (1–2), 32–36.

Hovius, N., Stark, C.P., Tutton, M.A., Abbott, L.D., 1998. Landslide-driven drainage network evolution in a pre-steady-state mountain belt: Finisterre Mountains, Papua New Guinea. Geology 26, 1071–1074.

Isacks, B.L., 1988. Uplift of the central Andean Plateau and bending of the Bolivian Orocline. Journal of Geophysical Research 93 (B4), 3211–3231.

Jaillard, E., Hérail, G., Monfret, T., Días-Martínez, E., Baby, P., Lavenu, A., Dumont, J.-F., 2000. Tectonic evolution of the Andes of Ecuador, Peru, Bolivia and northernmost Chile. In: Cordani, U.J., Milani, E.J., Thornaz Filho, A., Campos, D.A. (Eds.), Tectonic evolution of South America: 31st International Geological Congress, Rio de Janeiro, Brazil, pp. 481–559.

Kirchner, J.W., Finkel, R.C., Riebe, C.S., Granger, D.E., Clayton, J.L., King, J.G., Megahan, W.F., 2001. Mountain erosion over 10 yr, 10 ky., and 10 m.y. time scales. Geology 29 (7), 591–594.

Kober, F., Ivy-Ochs, S., Schlunegger, F., Baur, H., Kubik, P.W., Wieler, R., 2007. Denudation rates and a topography-driven rainfall threshold in northern Chile: multiple cosmogenic nuclide data and sediment yield budgets. Geomorphology 83, 97–120.

Kober, F., Ivy-Ochs, S., Zeilinger, G., Schlunegger, F., Kubik, P.W., Baur, H., Wieler, R., 2009. Complex multiple cosmogenic nuclide concentration and histories in the arid Rio Lluta catchment, northern Chile. Earth Surface Processes and Landforms 34, 398–412.

Kohl, C.P., Nishiizumi, K., 1992. Chemical isolation of quartz for measurement of in situ-produced cosmogenic nuclides. Geochimica et Cosmochimica Acta 56 (9), 3583–3587.

Korup, O., 2006. Rock-slope failure and the river long profile. Geology 34 (1), 45–48.

Mettier, R., Schlunegger, F., Schneider, H., Rieke-Zapp, D., Schwab, M., 2009. Relationships between landscape morphology, climate and surface erosion in northern Peru at 5°S latitude. International Journal of Earth Sciences 98 (8), 2009–2022.

Molnar, P., 2001. Climate change, flooding in arid environments, and erosion rates. Geology 29, 1071–1074.

Mourier, T., Laj, C., Megard, F., Roperch, P., Mitouard, P., Farfan Medrano, A., 1988. An accreted continental terrane in northwestern Peru. Earth and Planetary Science Letters 88 (1–2), 182–192.

Nishiizumi, K., Imamura, M., Caffee, M.W., Southon, J.R., Finkel, R.C., McAninch, J., 2007. Absolute calibration of Be-10 AMS standards. Nuclear Instruments & Methods in Physics Research Section B: Beam Interactions with Materials and Atoms 258 (2), 403–413.

Norton, K.P., Vanacker, V., 2009. Effects of terrain smoothing on topographic shielding correction factors for cosmogenic nuclide-derived estimates of basin-averaged denudation rates. Earth Surface Processes and Landforms 34 (1), 145–154.

Pedoja, K., Ortlieb, L., Dumont, J.-F., Lamothe, J.-F., Ghaleb, B., Auclair, M., Labrousse, B., 2006. Quaternary coastal uplift along the Talara Arc (Ecuador, Northern Peru) from new marine terrace data. Marine Geology 228 (1–4), 73–91.

Perron, T.J., Dietrich, W.E., Kirchner, J.W., 2008. Controls on the spacing of first-order valleys. Journal of Geophysical Research 113, F04016. doi:10.1029/2007F00977.

Quinn, W.H., 1992. A study of Southern Oscillation-related climatic activity for A.D. 622–1900 incorporating Nile River flood data. In: Diaz, H.F., Markgraf, V. (Eds.), El Niño Historical and Paleoclimatic Aspects of the Southern Oscillation. Cambridge University Press, Cambridge, UK, pp. 119–149.

Quinn, W.H., Neal, V.T., Demayolo, S.E.A., 1987. El Niño occurrences over the past four and a half centuries. Journal of Geophysical Research 92 (C13), 14449–14461.

Rasmusson, E.M., Carpenter, T.H., 1982. Variations in tropical sea surface temperature and surface wind fields associated with the Southern Oscillation/El Niño. Monthly Weather Review 110, 354–384.

Rein, B., 2007. How do the 1982/83 and 1997/98 El Niños rank in a geological record from Peru? Quaternary International 161, 56–66.

Reiners, P.W., Ehlers, T.A., Mitchell, S.G., Montgomery, D.R., 2003. Coupled spatial variations in precipitation and long-term erosion rates across the Washington Cascades. Nature 426 (6967), 645–647.

Reyes, L., Caldas, J., 1987. Geología de los cuadrangulós de Las Playas, La Tina, Las Lomas, Ayabaca, San Antonio, Chulucanas, Morropón, Huancabamba, Olmos y Pomahuaca. Instituto Geológico Minero y Metalúrgico, boletín no. 39, Lima, Perú. 83 pp.

Riebe, C.S., Kirchner, J.W., Granger, D.E., Finkel, R.C., 2000. Erosional equilibrium and disequilibrium in the Sierra Nevada, inferred from cosmogenic 26Al and 10Be in alluvial sediment. Geology 28 (9), 803–806.

Riebe, C.S., Kirchner, J.W., Finkel, R.C., 2004. Erosional and climatic effects on long-term chemical weathering rates in granitic landscapes spanning diverse climate regimes. Earth and Planetary Science Letters 224 (3–4), 547–562.

Rodbell, D.T., Seltzer, G.O., Anderson, D.M., Abbott, M.B., Enfield, D.B., Newman, J.H., 1999. An 15,000 year record of El Niño-driven alluviation in Southwestern Ecuador. Science 283, 516–520.

Roe, G.H., Montgomery, D.R., Hallet, B., 2002. Effects of orographic precipitation variations on the concavity of steady-state river profiles. Geology 30, 143–146.

Rogers, S.S., Sandweiss, D.H., Maasch, K.A., Belknap, D.F., Agouris, P., 2004. Coastal change and beach ridges along the northwest coast of Peru: image and GIS analysis of the Chira, Piura, and Colan beach-ridge plains. Journal of Coastal Research 20 (4), 1102–1125.

Rollins, H.B., James, B., Richardson, I., Sandweiss, D.H., 1986. The birth of El Niño: geoarchaeological evidence and implications. Geoarchaeology: An International Journal 1 (1), 3–15.

Safran, E.B., Bierman, P.R., Alto, R., Dunne, T., Whipple, K.X., Caffee, M., 2005. Erosion rates driven by channel network incision in the Bolivian Andes. Earth Surface Processes and Landforms 30 (8), 1007–1024.

Sandweiss, D.H., 2003. Terminal Pleistocene through mid-Holocene archaeological sites as paleoclimatic archives for the Peruvian coast. Palaeogeography Palaeoclimatology Palaeoecology 194 (1–3), 23–40.

Sandweiss, D.H., Maasch, K.A., Burger, R.L., Richardson, J.B., Rollins, H.B., Clement, A., 2001. Variation in Holocene El Nino frequencies: climate records and cultural consequences in ancient Peru. Geology 29 (7), 603–606.

Schildgen, T.F., Hodges, K.V., Whipple, K.X., Reiners, P.W., Pringle, M.S., 2007. Uplift of the western margin of the Andean plateau revealed from canyon incision history, southern Peru. Geology 35 (6), 523–526.

Schlunegger, F., Zeilinger, G., Kounov, A., Kober, F., Hüsser, B., 2006. Scale of relief growth in the forearc in the Andes of Northern Chile (Arica latitude, 18°S). Terra Nova 18, 217–223.

Schneider, H., Schwab, M., Schlunegger, F., 2008. Channelized and hillslope sediment transport and the geomorphology of mountain belts. International Journal of Earth Sciences 97 (1), 179–192.

Steffen, D., Schlunegger, F., Preusser, F., 2009. Drainage basin response to climate change in the Pisco valley, Peru. Geology 37, 491–494.

Stone, J.O., 2000. Air pressure and cosmogenic isotope production. Journal of Geophysical Research 105 (B10), 23,753–23,759.

Summerfield, M.A., Hulton, N.J., 1994. Natural controls of fluvial denudation rates in major world drainage basins. Journal of Geophysical Research 99 (B7), 13871–13883.

Tucker, G.E., Slingerland, R., 1997. Drainage basin responses to climate change. Water Resources Research 33, 2031–2047.

Van der Beek, P., Braun, J., 1998. Numerical modeling of landscape evolution on geological time-scales: a parameter analysis and comparison with the south-eastern highlands of Australia. Basin Research 10, 49–68.

von Blanckenburg, F., 2005. The control mechanisms of erosion and weathering at basin scale from cosmogenic nuclides in river sediment. Earth and Planetary Science Letters 237, 462–479.

von Blanckenburg, F., Hewawasam, T., Kubik, P.W., 2004. Cosmogenic nuclide evidence for low weathering and denudation in the wet, tropical highlands of Sri Lanka. Journal of Geophysical Research 109 (F3) pages.

Wells, L.E., Noller, J.S., 1997. Determining the early history of El Niño. Science 276, 965–967.
Whipple, K.X., 2004. Bedrock rivers and the geomorphology of active orogens. Annual Review of Earth and Planetary Sciences 32, 151–185.
Whipple, K.X., 2009. The influence of climate on the tectonic evolution of mountain belts. Nature Geoscience 2, 97–104. doi:10.1038/NGEO413.
Whipple, K.X., Tucker, G.E., 1999. Dynamics of the stream-power river incision model: implications for height limits of mountain ranges, landscape response timescales, and research needs. Journal of Geophysical Research 104, 17661–17674.
Whipple, K.X., Kirby, E., Brocklehurst, S.H., 1999. Geomorphic limits to climate-induced increases in topographic relief. Nature 401, 39–43.
Wobus, C., Whipple, K.X., Kirby, E., Snyder, N., Johnson, J., Spyroplou, K., Crosby, B., Sheehan, D., 2006. In: Willett, S.D., Hovius, N., Brandon, M.T., Fisher, D.M. (Eds.), Tectonics from topography: procedures, promise, and pitfalls: Tectonics, Climate, and Landscape Evolution: Special Paper 398, Penrose Conference Series, Geological Society of America, Boulder, Colorado, pp. 55–74.
Wolman, W.M., Miller, J.P., 1960. Magnitude and frequency of forces in geomorphic processes. The Journal of Geology 68, 54–74.
Woodman, R., 1998. El Fenomeno El Niño y el Clima en el Perú, El Perú en los Albores del Siglo XXI/2 (Ciclo de Conferencias 1997–1998): Ediciones del Congreso del Perú, Lima, Perú, pp. 201–242.
Zaprowski, B., Pazzaglia, F.J., Evenson, E.B., 2005. Influences on profile concavity and river incision. Journal of Geophysical Research 110, F03004. doi:10.1029/2004JF000138.
Zeilinger, G., Schlunegger, F., 2007. Possible flexural accommodation on the eastern edge of the Altiplano in relation to focussed erosion in the Rio La Paz drainage system. Terra Nova 19, 373–380.